Nonlinear Dyn
https://doi.org/10.1007/s11071-025-11537-x

RESEARCH

Nonlinear dynamics and potential of an energy harvester based on a horizontal axis flywheel

Giuseppe Giorgi · Giuseppe Habib · Fabio Carapellese

Received: 2 May 2025 / Accepted: 27 June 2025

Abstract This paper investigates the potential and nonlinear dynamics of an inertial energy harvester based on a horizontal axis flywheel enclosed in a floating hull. Two numerical modeling approaches are presented and compared, namely a block-based model and an analytical Lagrangian model using quasi-coordinates. The free (unloaded) response to external excitation is first analyzed to qualify the type of response of the system, especially focusing on the operational regions that may lead to periodic or chaotic response, and quantify the related potential for energy extraction. Secondly, the effect of the action of energy conversion is considered via the inclusion of a slowly variable power take-off damping, particularly evaluating if and how it undermines the underlying potential of the unloaded system; regimes of oscillation, rotation, and chaos are particularly highlighted, considering their effectiveness for power production. Periodic rotational solutions are the most promising for energy harvesting and are achievable for a wide range of excitation conditions; however, the sensitivity of optimal parameters and abrupt changes of performance between periodic and chaotic regions pose a challenge, calling for robust optimization design and optimal control.

Keywords Mechanical energy harvester · Gyroscope · wave energy · Quasi-coordinates · Chaos · Nonlinear vibration

1 Introduction

The increasing global energy demand poses a significant challenge to the sustainability of current energy systems, largely based on fossil fuels [1]. This scenario has accelerated efforts to transition toward renewable energy sources that can ensure energy security, reduce environmental impacts, and support long-term sustainability goals [2]. Among the various renewable energy options, wave energy is particularly promising due to its vast, yet underexploited, potential [3]. Since oceans cover a major part of the Earth's surface, the continuous motion of waves represents a considerable source of energy that could play a key role in diversifying the global energy mix [4,5]. In comparison to solar and wind energy, wave energy offers higher predictability and energy density, making it a particularly attractive

G. Giorgi (✉) · F. Carapellese
Marine Offshore Renewable Energy Lab (MOREnergy Lab), Department of Mechanical amd Aerospace Engineering (DIMEAS), Politecnico di Torino, Corso Duca degli Abruzzi 24, Turin 10129, Italy
e-mail: giuseppe.giorgi@polito.it

F. Carapellese
e-mail: fabio.carapellese@polito.it

G. Habib
Department of Applied Mechanics, MTA-BME Lendület Global Dynamics Research Group, Faculty of Mechanical Engineer, Budapest University of Technology and Economics, Műegyetem rkp. 3, Budapest 1111, Hungary
e-mail: habib@mm.bme.hu

option for consistent and reliable renewable power generation [6].

Wave energy converters (WECs) are an essential tool to harvest ocean wave energy; they are designed to capture the kinetic energy of waves and transform it into electricity [7]. WECs are typically categorized as oscillating water columns [8], point absorbers [6,9], and attenuators [10], each with unique mechanisms for energy extraction and conversion [7]. Current research in WEC technology emphasizes improving energy capture efficiency, enhancing durability in harsh marine environments, and reducing costs [11] to enable broader deployment [12].

This paper focuses on the inertial class of WECs, which has the main benefit of no moving parts in contact with seawater, providing a significant advantage in harsh marine environments. Passive inertial WECs typically operate based on the pendulum principle [13], as exemplified by devices such as the PeWEC [14], the SEAREV [15], and the AMOG [6]. Alternatively, some systems rely on a sliding mass that interacts inertially with a floating structure, such as the VIWEC [16], which features a vertical sliding mass enclosed within a hull, or the E-device [17], which employs a mass sliding along a horizontal plane. Another option for the inertial mechanical coupling is to exploit the gyroscope effect of a flywheel rotating around a vertical axis [18–20]: the gyroscopic effect provides the mechanical coupling, while the vertical axis of the flywheel naturally guarantees a gravitational restoring torque. Such systems, both passive and active, have the common likely drawback of being highly sensitive to the direction of wave propagation [21]; to overcome this limitation, some inertial WECs have incorporated more complex mechanisms to exploit multiple degrees of freedoms (DoFs) [22]. In fact, the severity of directionality (either wave spreading or mean wave direction) is substantial: [23] quantifies the effect of wave spreading from 10% to 20% on the estimation of productivity for a submerged point absorber, while [24] quantifies up to 50% overestimation caused by neglecting the wave direction for a prismatic inertial device. Finally, considering a vertical-axis gyroscope-based WEC, [25] estimates that rendering the device in-sensitive to the wave direction leads to increases between 19.5% and 39.7% of productivity, depending on the installation site.

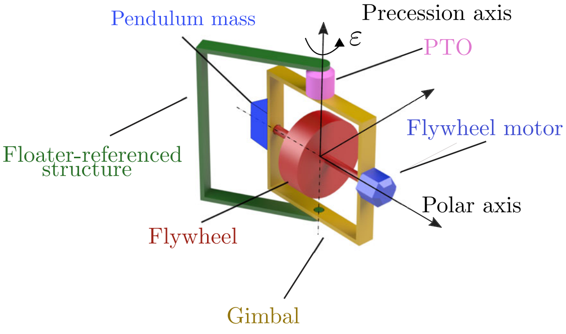

Fig. 1 Schematic representation of the vertical-axis gyroscopic system: The green structure is fixed on the floating hull and has the role of holding the yellow gimbal and a pink power take-off system on the precession axis; the role of the PTO is to convert mechanical energy to electricity, while the role of the gimbal is to hold the red flywheel, which is kept in rotation by the dark blue flywheel motor on the polar axis; the light blue pendulum mass has the role to avoid the lock-in of the gimbal

This paper proposes an implementation of a gyroscope-based WEC with a horizontal axis of rotation, such that it is insensitive to the direction of propagation of the incoming wave. Rotary energy harvesters have been extensively studied for various applications [26]; the concept offers scalability, potentially adaptable to various power requirements and wave climate conditions, making it a versatile approach for wave energy harvesting [27].

The proposed system is a horizontal axis flywheel WEC, shown in Fig. 1, consisting of a flywheel attached to a gimbal, with an eccentric mass to provide restoring stiffness, otherwise missing [28]. The system is subject to a based excitation, simulating the referenced floater motion, activated by the wave impact. The main objective of this study is to analyze the system dynamics, aiming to identify stable motion regimes, their advantages and drawbacks for energy harvesting, and evaluate the system's robustness against parameter variations. Similar nonlinear oscillations, subharmonic and chaotic regimes can also be observed in other energy harvesting mechanisms in the literature [29]. Results in this paper reveal an intricate alternation of rotary, periodic and chaotic motions, depending on the system parameters and wave excitation characteristics. Achieving stable rotary motion seems to be crucial for maximizing energy harvesting, which requires careful system's parameters tuning.

The remaining part of the paper is organized as follows. Sect. 2 describes the working principle of the system. Sect. 3 introduces the mechanical model and derives equations governing its dynamics, both through analytical methods and multi-body software. Sect. 4

presents the results of the numerical investigation and discusses their implications. Finally, Sect. 5 summarizes the study's conclusions, highlighting the advantages and limitations of the proposed system, and outlining possible future developments.

2 Working Principle of the Mechanism

Inertial energy harvester exploit the mechanical coupling between a relatively heavy object and its enclosing hull: as the floater moves subject to external excitation, the inner mass reacts and drives a power take-off (PTO) system [30]. Such a mechanical coupling can be passive or active. Passive coupling refers to a condition where no energy is required to activate the coupling, which therefore exists thanks only to the inherent inertial properties of the reacting mass; this is the case of pendulum-based harvesters. On the other hand, active coupling refers to a condition where energy is required to activate the coupling; this is the case of flywheels, which activate the gyroscopic effect via their rotational momentum. Such losses are mainly due to friction at the bearings and aerodynamic friction at the surface of the spinning flywheel [31]; the intensity of the losses depends on the mechanical configuration (e.g., bearing diameters, inter-axis), the spinning rotation of the flywheel, and the optional presence of a vacuum chamber surrounding the flywheel to reduce the net pressure [31].

State of the art gyroscope-based systems for WECs are typically using a flywheel with vertical axis [19, 22]. One of the main disadvantage of such systems is the sensitivity to the wave direction and the spreading factor of the incoming excitation wave [22,32]; in fact, a vertical-axis flywheel has a PTO on the horizontal axis: only wave traveling parallel to the PTO axis have the potential to fully excite the system, while energy from or spread over different directions is not efficiently intercepted. To counter this major limitation, this paper proposes a flywheel with horizontal axis, such that the PTO is installed on a vertical axis.

Figure 1 shows the schematic representation of the inner mechanism, which is fixed upon the floating hull through the green structure. Let us consider, for simplicity, unidirectional waves: when the incoming wave reaches the floating hull, it rotates about an axis perpendicular to the wave propagation; thus, also the floater-referenced structure rotates along with the hull. If such a rotation is not parallel to the flywheel motor axis (polar axis), then a gyroscopic torque is generated on the PTO axis (precession axis), thus extracting mechanical energy. If the floater's rotation is parallel to the polar axis, no gyroscopic torque exists and there may be a lock-in phenomenon; to avoid this, a pendulum mass is also included: a hull rotation parallel (but not coincident) with the polar axis would make the gimbal rotate due to an unbalanced pendulum mass, thus making the polar axis rotate and become incident with the hull's rotation.

A potential drawback of the system is the absence of an equilibrium position of the gimbal when the floater is at rest, nor a natural period of the precession axis, due to the absence of a restoring element. This may induce complex dynamics, potentially not convenient for practical implementation as energy harvester. Therefore, the focus of this paper is to study the dynamics of the system, with and without energy extraction at the PTO system, with the specific pragmatic perspective of energy harvesting. The inertial properties have been chosen based on existing gyroscope-based WECs [22], and are tabulated in Table 1. A small friction damping ($2 \cdot 10^3$ Nmrad/s) is also included on the PTO axis, to avoid unrealistic chaos with little practical meaning. This friction also encompasses bearings and aerodynamic losses, which are not modeled explicitly; such losses are relatively small during steady-state operations, when the flywheel speed is constant [31].

It is worth noting that the simplified assumption of unidirectional waves is employed in this paper for clarity in analyzing the fundamental nonlinear dynamics and potential for energy harvesting. However, real ocean environments are characterized by complex multidirectional wave spectra. While a full analysis of multidirectional wave interaction is beyond the scope of this paper, the proposed horizontal-axis flywheel configuration is inherently designed to mitigate the directional sensitivity observed in traditional vertical-axis gyroscopic WECs. By having the Power Take-Off (PTO) system installed on a vertical axis, the device aims to efficiently intercept energy regardless of the incoming wave direction. Future work will investigate the system's performance and dynamic behavior under more realistic multidirectional wave conditions, potentially through advanced numerical modeling that incorporates wave-structure interaction and directional spreading.

Table 1 Physical parameters of the system: mass (m) and inertia (I) of each body around its respective center of gravity

Body	Property	Value	Unit
Flywheel	m_f	7439	kg
	I_{f_x}	1303.88	kg m^2
	I_{f_y}	1113.04	kg m^2
	I_{f_z}	1113.04	kg m^2
Gimbal	m_s	3969	kg
	I_{s_x}	2852.39	kg m^2
	I_{s_y}	5320.31	kg m^2
	I_{s_z}	2525.21	kg m^2
Pendulum mass	m_p	120	kg
	I_{p_x}	2.725	kg m^2
	I_{p_y}	2.9	kg m^2
	I_{p_z}	0.625	kg m^2

3 Analytical Model Computation

This section presents the methodology for deriving the equation of motion that governs the dynamics of the gyroscope system with respect to its precession axis. The approach begins with the definition of the kinematic elements of the system and progresses to the application of Lagrange's equations. The resulting dynamic model captures the response of the gyroscope, influenced primarily by externally imposed motion, leading to a series of parametric excitations. A similar implementation of this analytical model has been preliminarily validated through experimental testing [33], considering an alternative gyroscope-based mechanism, thus building confidence on the validity of the numerical approach; a targeted experimental validation for the very system proposed in this paper is beyond the scope of work. However, an equivalent Simscape (Matlab Simulink) model is also defined, in order to cross-verify the implementation of the analytical model. Note that the Simscape model, which implements a block-oriented modeling approach, is virtually equivalent to the analytical model; however, the analytical approach provides several advantages, on top of the higher computational efficiency, as elaborated hereafter.

Firstly, the analytical model is more transparent and is able to provide valuable insights into dominant physical phenomena. Moreover, it enables the derivation of both linear and intermediate nonlinear approximations [34], which are essential for design techniques, such as optimization methods, particularly adopted in the design of WEC systems [16] and sophisticated control strategies [35,36] aimed at maximizing the extracted power. These methodologies often rely on the analytical formulation, with the choice of the specific modeling approach depending on the selected design strategy. A linear model offers a computationally efficient framework for optimization purposes and enables the application of Linear Time-Invariant (LTI) control strategies [37,38]. However, for design requirements demanding higher accuracy, a partially nonlinear model proves more suitable, as it allows for nonlinear control strategies [39] and refined system design [40,41]. This approach strikes a balance between computational efficiency and model accuracy, making it more practical than a fully nonlinear representation. All the methodologies mentioned are not directly compatible with the Simscape simulation, which represents the system dynamics as a black box and requires the computation of an analytical model.

3.1 Kinematic representation

This section derives the fundamental nonlinear mathematical model governing the dynamics of a vertical-axis gyroscopic system. In particular, the gyroscope is externally actuated through a structure referenced to as platform. In detail, the gyroscope system can be decomposed into three main bodies: the flywheel, the gimbal, and the pendulum system. The flywheel, whose spinning velocity ($\dot{\varphi}$) is constant and user-defined, induces the rotation of the gimbal around the precession axis by an angle $\varepsilon : t \mapsto \varepsilon \in \mathbb{R}$ due to the gyroscopic effect. This effect is generated by the interaction between the flywheel's rotational velocity and the platform's rotational motion. The pendulum mass prevents the system from locking by introducing a reactive component.

As relative motion between the referenced structure and the mechanism occurs during operation, a suitable set of reference frames is introduced [42], as detailed in Fig. 2. They can be described as follows:

- $\mathcal{R}(OXYZ)$: the inertial reference frame;
- $\mathcal{R}(\mathcal{O}'xyz)$: the frame fixed to the floater-referenced structure, with the x-axis aligned with the incoming wave direction;
- $\mathcal{R}(\mathcal{G}\Xi\mathcal{H}\mathcal{Z})$: the frame parallel to $\mathcal{R}(\mathcal{O}'xyz)$, translated by the vector $r_0 \in \mathbb{R}^3$, defined as $r_0 = [x_0 \quad y_0 \quad z_0]^\mathsf{T}$, from the floater-referenced structure

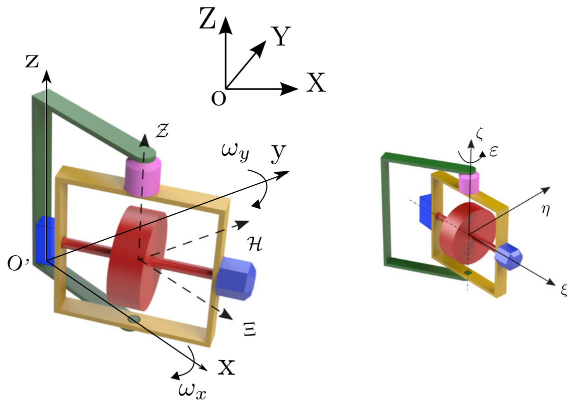

Fig. 2 Schematic representation of the frames of reference to describe the vertical-axis gyroscopic system

to the center of gravity (CoG) of the conversion unit;

- $\mathcal{R}(\mathcal{G}\xi\eta\zeta)$: the gimbal-fixed reference frame, which follows the gyroscope precession motion.

Although the referenced structure can be externally excited over a complete set of DoFs, both linear and angular, as introduced in [42], in this work, the derivation of the analytical equations is restricted to the parametric excitation induced exclusively on the angular DoF, referenced to $\mathcal{R}(\mathcal{O}'xyz)$. For this purpose, we define the vector $\Phi \in \mathbb{R}^3$ of generalized coordinates related to the platform

$$\Phi = \begin{bmatrix}\delta & \theta & \psi\end{bmatrix}^{\mathsf{T}},$$

where $\delta : t \mapsto \delta \in \mathbb{R}$, $\theta : t \mapsto \theta \in \mathbb{R}$, and $\psi : t \mapsto \psi \in \mathbb{R}$ represent the externally induced roll, pitch, and yaw rotations, respectively.

With the reference frames defined above, we derive the nonlinear equation of motion, linked to the gyroscope DoF ε in terms of *quasi-coordinates* (see, e.g., [43,44]), allowing us to map the external excitation motion Φ referenced to $\mathcal{R}(\mathcal{O}'xyz)$ onto the gyroscope-fixed reference frame $\mathcal{R}(\mathcal{G}\xi\eta\zeta)$. The vector of quasi-coordinates in the mapping from $\mathcal{R}(\mathcal{O}'xyz) \mapsto \mathcal{R}(\mathcal{G}\xi\eta\zeta)$, is defined as $\Omega_T : t \mapsto \Omega_T \in \mathbb{R}^3$, with

$$\Omega_T = R(\varepsilon, \hat{\zeta})^{\mathsf{T}} D\dot{\Phi}, \tag{1}$$

where $R(\varepsilon, \hat{\zeta})$ denotes the rotation matrix of angle ε with respect to the unit vector $\hat{\zeta}$ along the ζ-axis, and $D \in \mathbb{R}^{3\times 3}$ is the inverse of the analytical Jacobian matrix, as defined in [45]. Moreover, since a linear velocity is induced in a rigid body when motion occurs around an axis different from the referenced rotation axis, in $\mathcal{R}(\mathcal{G}\xi\eta\zeta)$ it can be expressed as follows:

$$V_T = -R(\varepsilon, \hat{\zeta})^{\mathsf{T}} \tilde{r_0}^1 D\dot{\Phi}, \tag{2}$$

Thus, the total velocity $\Omega_G : t \mapsto \Omega_G \in \mathbb{R}^3$, defined as $\Omega_G = [\Omega_\xi \quad \Omega_\eta \quad \Omega_\zeta]^{\mathsf{T}}$, links the mapped platform velocity in $\mathcal{R}(\mathcal{G}\xi\eta\zeta)$ to the proper velocity of the gyroscope, $\dot{\varepsilon}$, while the linear velocity remains invariant:

$$\begin{bmatrix} V_G \\ \Omega_G \end{bmatrix} = \begin{bmatrix} -R(\varepsilon, \hat{\xi})^{\mathsf{T}} \tilde{r} D & 0 \\ R(\varepsilon, \hat{\xi})^{\mathsf{T}} D & \tilde{I} \end{bmatrix} \begin{bmatrix} \dot{\Phi} \\ \dot{\varepsilon} \end{bmatrix}, \tag{3}$$

where $\tilde{I} = [0 \quad 0 \quad 1]^{\mathsf{T}}$ incorporates the precession velocity into the angular velocity component related to the precession axis unit vector $\hat{\zeta}$.

All excitation components related to the prescribed platform motion are defined in the gyroscope reference frame. Now, we can define the proper velocity for each discrete body: the flywheel, pendulum, and gimbal. For the latter, the entire velocity vector corresponds to the velocity defined in Equation (3). While for the flywheel, an additional velocity component corresponding to its own rotation must be considered. The components of the total flywheel velocity $\Omega_F = [\Omega_{\xi'} \quad \Omega_{\eta'} \quad \Omega_{\zeta'}]^{\mathsf{T}}$ are given by:

$$\Omega_{\xi'} = \Omega_\xi, \qquad \Omega_{\eta'} = \Omega_\eta, \qquad \Omega_{\zeta'} = \Omega_\zeta + \dot{\varphi}, \tag{4}$$

where $\dot{\varphi}$ accounts for the flywheel rotation, which is superimposed on the mapped velocity in the gyroscope-fixed frame.

The total velocity vector of the pendulum, characterized by its linear velocity $V_P \in \mathbb{R}^3$ and angular velocity $\Omega_P \in \mathbb{R}^3$, defined in the reference frame $\mathcal{R}(\mathcal{G}\xi\eta\zeta)$ and based on the arm position vector with respect to the precession axis $l_0 = [l_p \quad 0 \quad 0]^{\mathsf{T}}$, is

$$\begin{bmatrix} V_P \\ \Omega_P \end{bmatrix} = \begin{bmatrix} I_3 & -\tilde{l_0}^2 \\ 0 & I_3 \end{bmatrix} \begin{bmatrix} V_G \\ \Omega_G \end{bmatrix}. \tag{5}$$

---

[1] the $\tilde{r_0}$ marks the skew-symmetric matrix associated with the r_0 vector.

The system's position is expressed with respect to the inertial frame using the position vector $p_m \in \mathbb{R}^3$, defined as:

$$p_m = T^1 T^2 l_0, \tag{6}$$

while the position of the flywheel and gimbal, sharing the same CoG, is given by:

$$p_g = T^1 r_0, \tag{7}$$

where the roto-translation matrices T^1 and T^2 are defined as:

$$T^1 = \begin{bmatrix} C & \begin{bmatrix} x \\ y \\ z \end{bmatrix} \\ 0 & 1 \end{bmatrix}, \quad T^2 = \begin{bmatrix} R(\varepsilon, \hat{\xi}) & \begin{bmatrix} x_0 \\ y_0 \\ z_0 \end{bmatrix} \\ 0 & 1 \end{bmatrix}. \tag{8}$$

Here, C is defined as the composition of rotation matrices, according to the roll, pitch and yaw convention:

$$C = R(\psi, \hat{z}) R(\vartheta, \hat{y}) R(\delta, \hat{x}). \tag{9}$$

3.2 Lagrange Approach for Quasi-Coordinates

With the kinematic description of the gyroscope system and the detailed velocity and position of each gyroscope component, as presented in Sect. 3.1, it is now possible to define the kinetic and potential energy of the system to derive the equations of motion using Lagrange's equations [46]. The extrapolated Lagrange equation for quasi-coordinates, related to the precession axis DoF, can be expressed as follows:

$$\begin{aligned} &\frac{d}{dt}\left(\frac{\partial \mathcal{T}}{\partial \omega_\zeta}\right) - \omega_\eta \frac{\partial \mathcal{T}}{\partial \omega_\xi} + \omega_\xi \frac{\partial \mathcal{T}}{\partial \omega_\eta} \\ &- v_\eta \frac{\partial \mathcal{T}}{\partial v_\xi} - v_\xi \frac{\partial \mathcal{T}}{\partial v_\eta} + \frac{\partial \mathcal{U}}{\partial \varepsilon} = f_{\text{pto}} + f_{\text{fric}} \end{aligned} \tag{10}$$

where $\mathcal{T}(\Omega_G) \in \mathbb{R}$ and $\mathcal{U}(\Phi) \in \mathbb{R}$ represent the system's kinetic and potential energy, respectively (the reader can refer to [42] for further details on the derivation of the kinetic and potential energy of the system). The term f_{pto} is introduced to describe the PTO dynamic action during the power extraction process. Specifically, the PTO control torque is defined in terms of the following passive parametric expression:

$$f_{\text{pto}} = -c_{PTO} \dot{\varepsilon}, \tag{11}$$

where $c_{PTO} \in \mathbb{R}^+$ is the control parameter of the PTO system, optimized to maximize energy extraction efficiency based on the frequency of wave excitation forces [47,48]. The application of such force is directly related to the extracted mechanical power $P_a \in \mathbb{R}^-$, defined as $P_a = f_{\text{pto}} \dot{\varepsilon}$.

The term $f_{\text{fric}} : t \mapsto f_{\text{fric}} \in \mathbb{R}$ represents the friction force acting on the PTO axis. Due to the coupling mechanism and generator, it is modeled as a simple viscous effect with the viscous parameter $c_f \in \mathbb{R}^+$, leading to $f_{\text{fric}} = c_f \dot{\varepsilon}$. Thus, the dynamic model of the gyroscope system is given by:

$$\begin{aligned} &I_\zeta \dot{\omega}_\zeta + m_p l_p \dot{v}_\eta + (I_\eta - I_\xi)\omega_\eta \omega_\xi - I_{f_x} \dot{\varphi} \omega_\eta \\ &\quad - m_p l_p v_\zeta \omega_\xi + m_p l_p v_\xi \omega_\zeta = f_{\text{pto}} + f_{\text{fric}}, \end{aligned} \tag{12}$$

where the introduced inertial elements are hereafter defined:

$$\begin{aligned} I_\xi &= I_{s_x} + I_{f_x} + I_{p_x}, \\ I_\eta &= I_{s_y} + I_{f_y} + I_{p_y} + m_p l_p^2, \\ I_\zeta &= I_{s_z} + I_{f_z} + I_{p_z} + m_p l_p^2. \end{aligned} \tag{13}$$

Note that Equation (12) is a nonlinear equation expressed in terms of quasi-coordinates, retained in this form for brevity but easily transformable into the generalized coordinate space using the relation provided in Sect. 3.1. The resulting equation is nonlinear and exhibits both parametric excitation and self-excitation effects [49].

The complete definition of the system dynamics depends on the modes of motion induced by the platform. To maintain generality, the formulation considers prescribed roll, pitch, and yaw motions as possible excitations. However, for simplicity, since the focus is on analyzing the nonlinear behavior of the gyroscope, the yaw mode is entirely neglected. The upcoming analysis prioritizes pitch motion, as it predominantly activates gyroscopic dynamics and is often coupled with roll motion for completeness.

---

[2] the $\tilde{l_0}$ marks the skew-symmetric matrix associated with the l_0 vector.

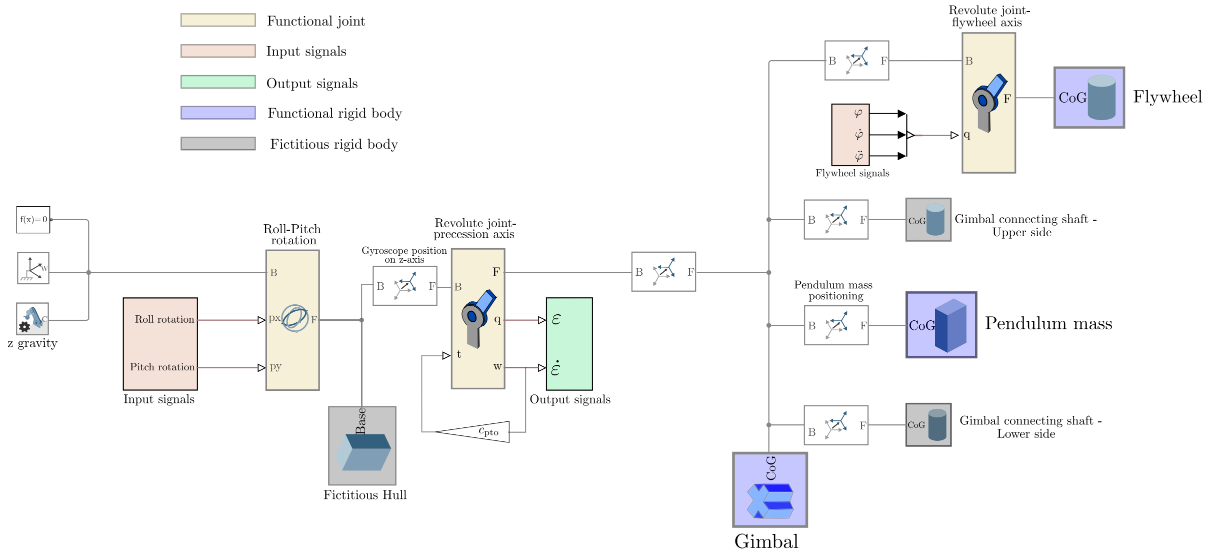

Fig. 3 A Simscape block diagram model for nonlinear simulation, highlighting the block types through different colors: light orange represents the joint elements, red denotes blocks containing the input signals, green indicates output signals, blue represents the rigid block system, and grey corresponds to the bodies included for visualization purposes

3.3 Block-Based Modeling

This section presents the benchmark block-based model, used for the verification of the analytical model: the Simscape simulation employs a block diagram approach to intuitively replicate the multibody dynamics of the gyroscopic system. The reader can refer to Fig. 3 for the corresponding block diagram [50]. This diagram provides a detailed representation of the simulation architecture of a vertical-axis gyroscope, illustrating the interaction between input-output signals, mechanical components, and control elements. To enhance readability, color-coded elements are used to differentiate system components: yellow for functional joints, red for input signals, green for output signals, and blue for rigid bodies.

The dynamics of the gyroscope system depend on its architectural configuration. Referring to Fig. 3, the system consists of three key rigid-body components, highlighted in blue: the flywheel, the pendulum mass, and the gimbal, all of which are interconnected through frame transformation blocks to ensure coordinated motion and structural integrity. The flywheel, modeled as a rigid body, serves as the primary source of angular momentum, maintaining its rotational energy. It is connected via a revolute joint that governs its axis of rotation, receiving controlled input signals such as its angular velocity $\dot{\varphi}$, which remains constant throughout the simulation to ensure stability and consistency in the modeled behavior.

4 Results

Results are articulated in this section, building towards a robust understanding of the primary nonlinear dynamics of the mechanism under consideration in this paper, with a particular emphasis on its potential applications in mechanical energy harvesting. The foundation of this study is built upon validating the mathematical models employed; to do so, Sect. 4.1 articulates a code-to-code comparison between the fully-nonlinear block-based Simscape model and the analytical Lagrangian model, considering both fully-nonlinear and linearized versions: consistency under compatible conditions will affirm the correctness of the numerical implementation, while discrepancies observed under conditions beyond the underlying assumptions will provide quantitative insights into the applicability and limitations of each model.

Following the code-to-code comparison, the fully-nonlinear model is adopted to pursue the analysis of the key nonlinear phenomena of interest. Firstly, Sect. 4.2

explores the free response of the system subject to external forcing, i.e. how the dynamics of the gimbal-flywheel assembly evolve without any energy extraction (undamped or unloaded response); this draws the boundaries of the potential for energy extraction, building upon the inherent nonlinear dynamics of the inertial mechanical system. Secondly, the damping action of a PTO system is introduced in Sect. 4.3: such a significant power dissipation, strictly required for the primary objective of energy harvesting, is quantitatively studied to evaluate if and how it undermines the underlying potential determined by the unloaded response of the system.

It is worth remarking that, since the objective of this paper is to study the nonlinear dynamics and potential of the inertial mechanism, the initial source of mechanical energy inducing the motion is neglected; therefore, the mechanical coupling between the gimbal-flywheel assembly and the outside world is not modeled. As a consequence, all of the results in Sect. 4 are produced by prescribing a given motion to the structure hosting the gimbal. This assumption is convenient and appropriate for the purposes of this study, since it enables a straightforward inference of causality between the prescribed kinematics and the nonlinear response of the inertial system. However, it is to be remarked that conclusions about resonance behavior or chaotic transition may, in principle, be affected by the wave-structure. Nonetheless, it can be expected that the overall observed dynamics remains qualitatively the same, despite the fluid-structure coupling is neglected; this is a reasonable assumption, based on the fact that the inertia of the hosting hull is usually relatively large and thus it is mostly affected by the wave forcing, rather than the inner mechanism. This expectation is consistent with available results in the literature, such as [14] for a pendulum inside a floating hull. Still, it is acknowledged that future studies, beyond the scope of this paper, are required to quantitatively address this topic.

4.1 Verification of the Numerical Models

The fully-nonlinear analytical model from Sect. 3.2 is compared to the block-based Simscape model from Sect. 3.3. In the Simscape model, the prescribed roll and pitch signals, δ and θ, along with their derivatives, are fed into a dedicated multi-DoF rotational joint, which, in conjunction with the hull block, replicates the prescribed motion imposed to the platform. This excitation parametrically influences the connected mechanism, triggering the gyroscopic effect through the revolute joint, which enables the sensing of the rotational motion ε. The joint is actively controlled via a dedicated actuation mechanism, where a proportional gain parameter, c_{PTO}, is applied to modulate the angular velocity, ensuring precise dynamic response and stability, as well as c_v to model the dissipative term due to the friction.

Initially, the system was simulated by exciting the gyroscope-connected platform with a prescribed pitch motion, directly triggering the gyroscopic effect. Specifically, the pitch excitation signal $\theta_{\text{test}} : t \mapsto \theta_{\text{test}} \in \mathbb{R}$ follows a harmonic function with an excitation frequency of $\omega_r = 1$ rad/s, which falls within the system's operational range. The excitation signal is defined as:

$$\theta_{\text{test}} = \theta_a \cos \omega_r t \tag{14}$$

where $\theta_a \in \mathbb{R}^+$ represents the amplitude of the harmonic signal, defined as $\theta_a = 8^\circ$ for this test. Moreover, the flywheel angular velocity is set to $\dot{\varphi} = 100$ rad/s, while the viscous friction parameter is assigned a value of $c_f = 2000$ Nms/rad, considering a simulation time of $T_{\text{sim}} = 140$ s.

Figure 4 shows that the two models exhibit a perfect match in terms of both angular velocity and power. In particular, several values of c_{PTO} values are considered to compare the pendulum dynamics in both uncontrolled conditions and under reasonable damping parameters, acting as a control mechanism during the system's operational phase. On the right side of Fig. 4, the phase diagram is plotted to highlight the nonlinear nature of the results. For the case of pitch motion alone, varying the damping parameter results in distinct dynamical behaviors. The phase portraits illustrate three different regimes: a chaotic response characterized by a complex and non-repetitive trajectory, a harmonic oscillatory motion with well-defined periodicity, and a signal exhibiting multiple subharmonics with different return periods. These variations highlight the influence of damping on the system's stability and periodicity.

Figure 5 presents a comparison between the analytical model, considering both pitch and roll as external excitation motions, and the Simscape model. An equivalent harmonic roll signal, $\delta_{\text{test}} : t \mapsto \delta_{\text{test}} \in \mathbb{R}$,

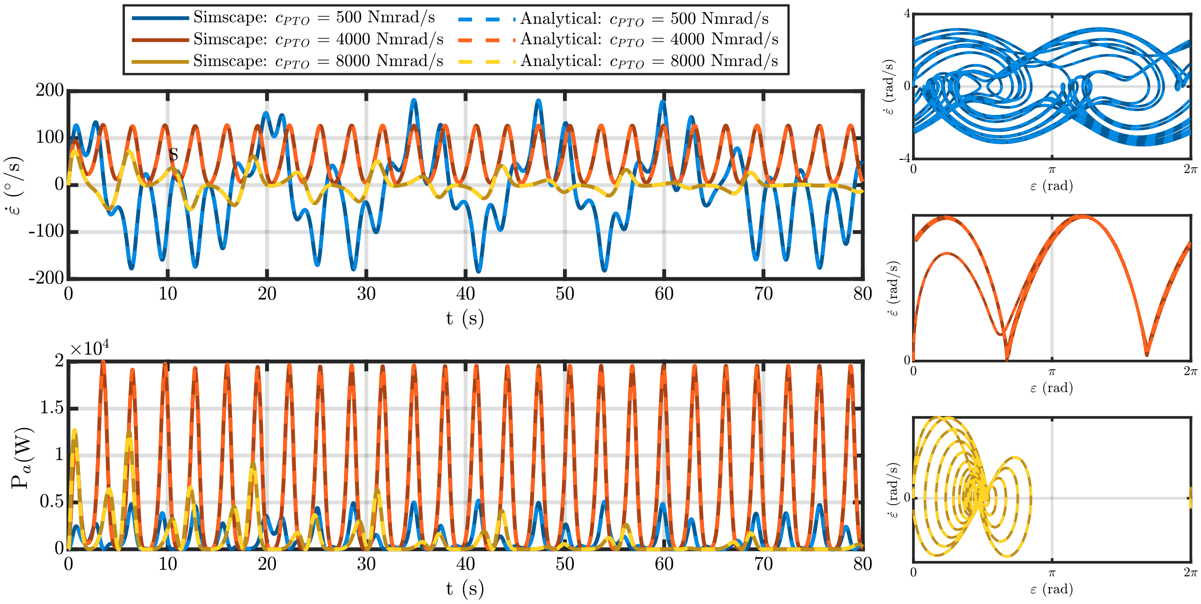

Fig. 4 Analytical model validation through the Simscape model, illustrating the precession velocity (top-left), the corresponding power (bottom-left), and the phase plot (right) for various PTO control parameters c_{pto}, simulating the pitch parametric excitation. The space plots on the right show the following dynamical regimes: chaotic (top), rotational (center), and oscillatory (bottom)

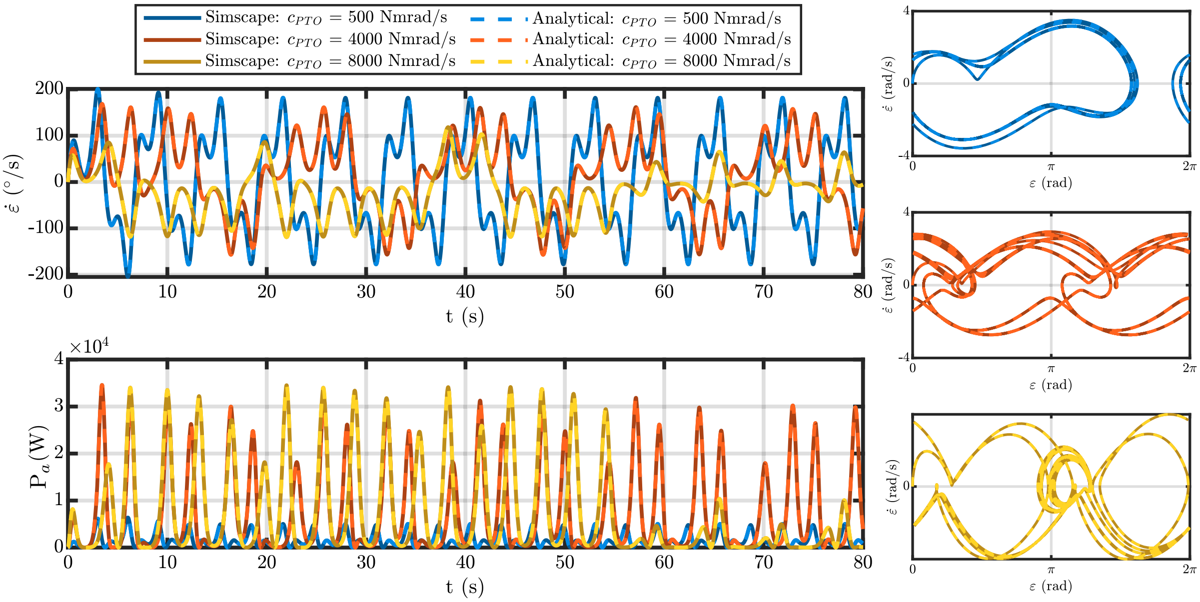

Fig. 5 Analytical model validation through the Simscape model, illustrating the precession velocity (top-left), the corresponding power (bottom-left), and the phase plot (right) for various PTO control parameters c_{PTO}, simulating the pitch and roll parametric excitation. All phase plots show periodic oscillatory regimes

is defined similarly to Equation (14), with an amplitude of $\delta_a = 8°$. The figure illustrates a perfect match between the two models in terms of angular velocity and power for the prescribed control parameter value, c_{PTO}. The phase portraits highlight the influence of damping on pitch motion dynamics, revealing a progressive reduction of higher-order harmonics. The first and second plots display a period-1 response with multiple harmonics. The third plot exhibits a subharmonic response, where nonlinear effects induce multi-periodicity. This analysis demonstrates how increasing damping simplifies the system's oscillatory behavior by gradually eliminating higher-frequency components, leading to a more regular dynamic response. Note that, as confirmed by the phase portraits in Fig. 4 and 5, the analytical model remains valid and consistent with the Simscape simulation even when the gyroscopic rotation exceeds π or completes a full turn, fully entering the nonlinear operating region. This demonstrates that the analytical formulation accurately captures the system's dynamics across the entire operating range, from small to large oscillations, and remains reliable beyond the small-oscillation regime.

4.1.1 Analysis on the linear system dynamics

The comparison between the full nonlinear model, as expressed in (12), and its linear counterpart is illustrated in Fig. 6. For this comparison, both exclusive pitch excitation and the simultaneous excitation of pitch and roll parameters are considered. Despite the specific nature of the imposed motion–whether in roll or pitch–the system's linear form retains a common harmonic structure. This can be understood from the formulation of the gyroscope's linear equation, which can be expressed as a second-order linear differential equation. The linearized expression, obtained through Jacobian linearization under the assumption of small rotation angles, is given by:

$$I_\zeta \ddot{\varepsilon} - m_p l_p z_0 \ddot{\delta} - I_{f_x} \dot{\varphi} \dot{\theta} + m_p l_p g \delta + f_{\text{fric}} = f_{\text{pto}}, \quad (15)$$

where this formulation highlights the dynamics influenced by pitch velocity, which activates the gyroscopic effect when the flywheel velocity is nonzero, as well as the reactive coupling with roll motion, which engages the pendulum mass.

Unlike its nonlinear counterpart, this equation features a single-harmonic excitation. In contrast to the nonlinear formulation, the linear counterpart does not exhibit parametric excitation but instead presents an explicit forcing term. Consequently, it can be rewritten in the canonical form of a damped, forced linear oscillator, as descibed in [51]:

$$I_\zeta \ddot{\varepsilon} + c_f \dot{\varepsilon} = \bar{A} \cos(\omega_r t) + \bar{B} \sin(\omega_r t), \quad (16)$$

where the excitation amplitudes are given by:

$$\bar{A} = I_{f_x} \dot{\varphi} \theta_a \omega_r \quad , \quad \bar{B} = -m_p l_p \delta_a (z_0 \omega_r^2 + g). \quad (17)$$

From the perspective of linear system theory, the equilibrium point of this system is at the origin ($\varepsilon = 0$), and its stability properties are determined by the coefficient c_f, which characterizes the damping effect. While the non-linear counterpart indicates that, for small perturbations, the system closely resembles its linear approximation. However, when considering wider oscillations, notable deviations emerge: for $\theta_a = 1°$, the system exhibits instability, with a divergent signal, whereas for $\theta_a = 8°$, after the transient phase, the system reaches a new equilibrium position distinct from zero. Note that, considering few approximations, Equation (12) can be written in a nonlinear Mathieu form, which can be expressed as:

$$\begin{bmatrix} \dot{\varepsilon} \\ \ddot{\varepsilon} \end{bmatrix} = \begin{bmatrix} 0 & 1 \\ -\beta \cos \tau & -c_f \end{bmatrix} \begin{bmatrix} \varepsilon \\ \dot{\varepsilon} \end{bmatrix} + \begin{bmatrix} 0 \\ F_{\text{ext}} \end{bmatrix} \quad (18)$$

where the external forcing term is given by:

$$F_{\text{ext}} = I_{f_x} \dot{\varphi} \theta_a \sin(\omega_r t)$$

with $\tau = \omega_r t - \pi/2$ and $\beta = m_p l_p g$. This formulation explains the results just described, as it enables a deeper analysis of the system's stability regions, particularly in identifying the conditions under which parametric resonance and equilibrium shifts occur in the nonlinear regime.

4.2 Free dynamics without energy extraction

The focus of this section is to explore the nonlinear response of the system, subject to external prescribed motion, without dissipation due to energy extraction. The fully-nonlinear Simscape model is used hereafter. Although the system is designed to be responsive to

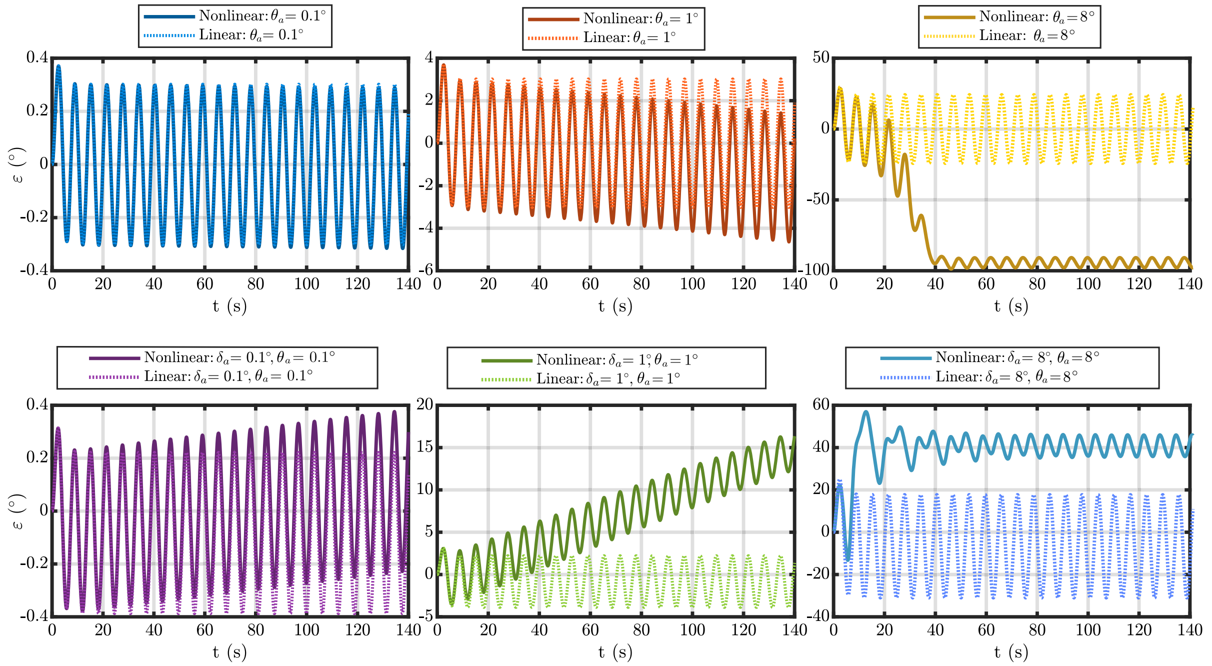

Fig. 6 Comparison of the ε time traces, according to the linear and nonlinear models, across different environmental conditions. The comparison includes exclusive pitch excitation (top) and combined equal pitch and roll parametric excitation (bottom). Three excitation amplitudes are considered: 0.1° (left), 1° (middle), 8° (right)

rotations of the supporting structure around any arbitrary horizontal axis, only the rotation ϑ around the y-axis has been considered for the following analysis; this choice makes the presentation and analysis of results simple and effective, while still being representative of the nonlinear phenomena under consideration in this paper. Therefore, the consequent set of independent variables is listed:

1. Period (T) or frequency ($f = 1/T$) of the prescribed pitch motion. Investigated ranges of periods are those of typical water waves: from 3 to 15 s [52].
2. Amplitude of the prescribed pitch motion: θ_a. Investigated ranges of pitching amplitude are those usually deemed reasonable, safe and feasible for floating objects: from 4° to 16°.
3. Damping at the PTO axis: c_{PTO}. In Sect. 4.2, c_{PTO} is set to zero, while Sect. 4.3 explores the range from zero to $2 \cdot 10^4$; the upper limit of this range has been defined based on the results. Note that c_{PTO} is added on top of the small additional damping term (c_f) that models the internal friction.

The main state variable for the analysis of the dynamics of the system is the velocity of the rotation at the PTO axis ($\dot{\varepsilon}$). Fig. 7 presents an example of three representative time series responses to harmonic prescribed motions, with amplitude of 8° and frequencies of 0.1 (top), 0.2 (middle), and 0.3 (bottom) Hz. Initial conditions are at rest (both amplitude and velocity equal to zero), such that the time window of the simulation includes both the transient and the steady state solution. Despite the prescribed motion is purely harmonic (mono-chromatic), the response signal is clearly richer, with multiple frequencies concurring to the total output. A periodic response is reached in the top and bottom time traces, while the response at 0.2 Hz seems to be chaotic. Alternating shadowed areas on the background are drawn at intervals equal to the period of the prescribed motion, thus highlighting the single (top) or double (bottom) periodicity of the output signal, respectively at 0.1 Hz and 0.3 Hz. Finally, it is worth noting that, when a periodic motion occurs, the transient response seems relatively short: about 2 excitation periods for the 0.1 Hz time trace, about 6 excitation periods for the 0.3 Hz, and lower than 20 s in general.

Fig. 7 Time trace responses to harmonic prescribed motion with amplitude of 8°, and frequency of 0.1 (top), 0.2 (middle), and 0.3 (bottom) Hz, with $c_{PTO} = 0$. Alternating shadowed areas on the background are drawn at intervals equal to the period of the prescribed motion

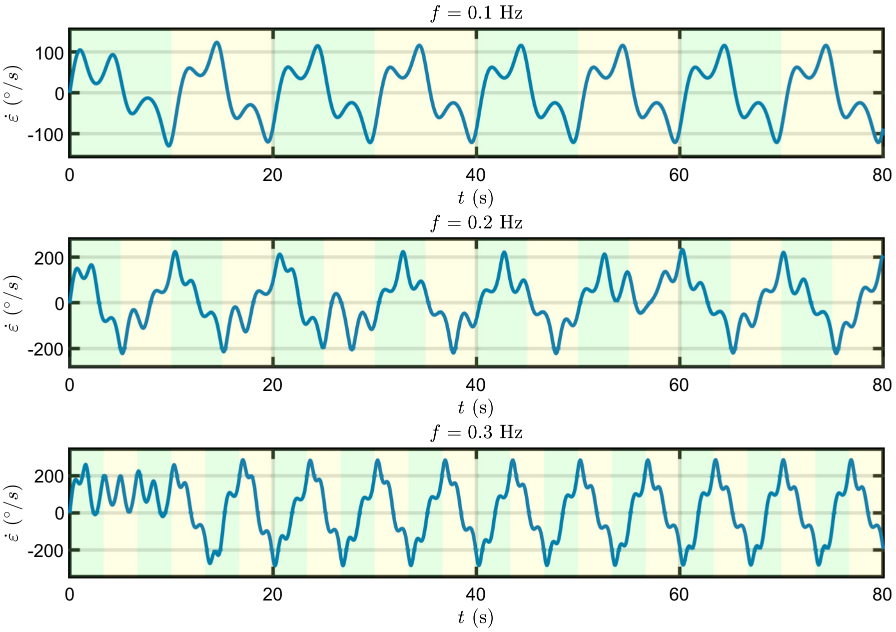

In order to study the response of the system across the whole range of frequencies of interest in a continuous way, a chirp signal is used as a prescribed motion, i.e. a harmonic function with frequency linearly varying with time [53]. Note that realistic waves would be panchromatic realizations of wave spectra (e.g. Pierson-Moskowitz [54] or JONSWAP [55]; however, using chirp signals is a compact and efficient way to investigate the response of a nonlinear dynamical system, often used for system identification [56] and experimental analysis [57]. Moreover, [58] shows that the nonlinear dynamics and behavior described via harmonic and chirp excitation is consistent and representative of the actual response to more realistic panchromatic waves; this is particularly true for floating systems with relatively fast transient responses, as the one considered in this paper (see Fig. 7), since the mechanism is most responsive to the local frequency content. This can be further verified, considering how much responses to up- and down-chirp signals overlap: the instantaneous frequency of a chirp signal can either increase or decrease, resulting in an up-chirp or down-chirp, respectively; exploring both directions of frequency variation allows for the identification of potential coexisting solutions [59]. Nevertheless, in order to properly appreciate the correct dynamics of the response, the simulation time must be long enough to ensure a slow and smooth modification of the instantaneous frequency; using a precautionary approach and based on the expected chaotic behavior, a very long simulation time is used, equal to 30,000 s, which is 2,000 times the longest period of 15 s and 10,000 times the shortest period of 3 s. Since the length of the swept wave periods is 12 s (from 3 s to 15 s, or vice versa), which linearly changes during a long 30,000-second window, it results that the rate of change of periods is 0.1 seconds every 250 seconds; this rate is effectively very slow, considering that, for example, Fig. 7 shows a transient response to harmonic waves elapsing withing the first 20 seconds. This builds confidence that, indeed, transient effects can be excluded from the analysis of the response to chirp signals.

The time series of the response ($\dot{\varepsilon}$) is processed to extrapolate a sequence of response amplitudes ($\dot{\varepsilon}_a$), defined as half the absolute value of the difference between two consecutive extremes (peak or trough). Similarly, a series of mean amplitudes ($\bar{\dot{\varepsilon}}$) can be computed as the absolute value of the sum of two consecutive extremes.

Figure 8 shows the time sequence of response amplitudes ($\dot{\varepsilon}_a$) subject to a down-chirp prescribed motions with forcing amplitude of 8°. The top graph of Fig. 8 shows $\dot{\varepsilon}_m$, which is $\dot{\varepsilon}$ sampled at every local maximum of the exciting prescribed motion. It can be readily noted that the central portion of the two graphs presents a chaotic behavior, while the regions at the

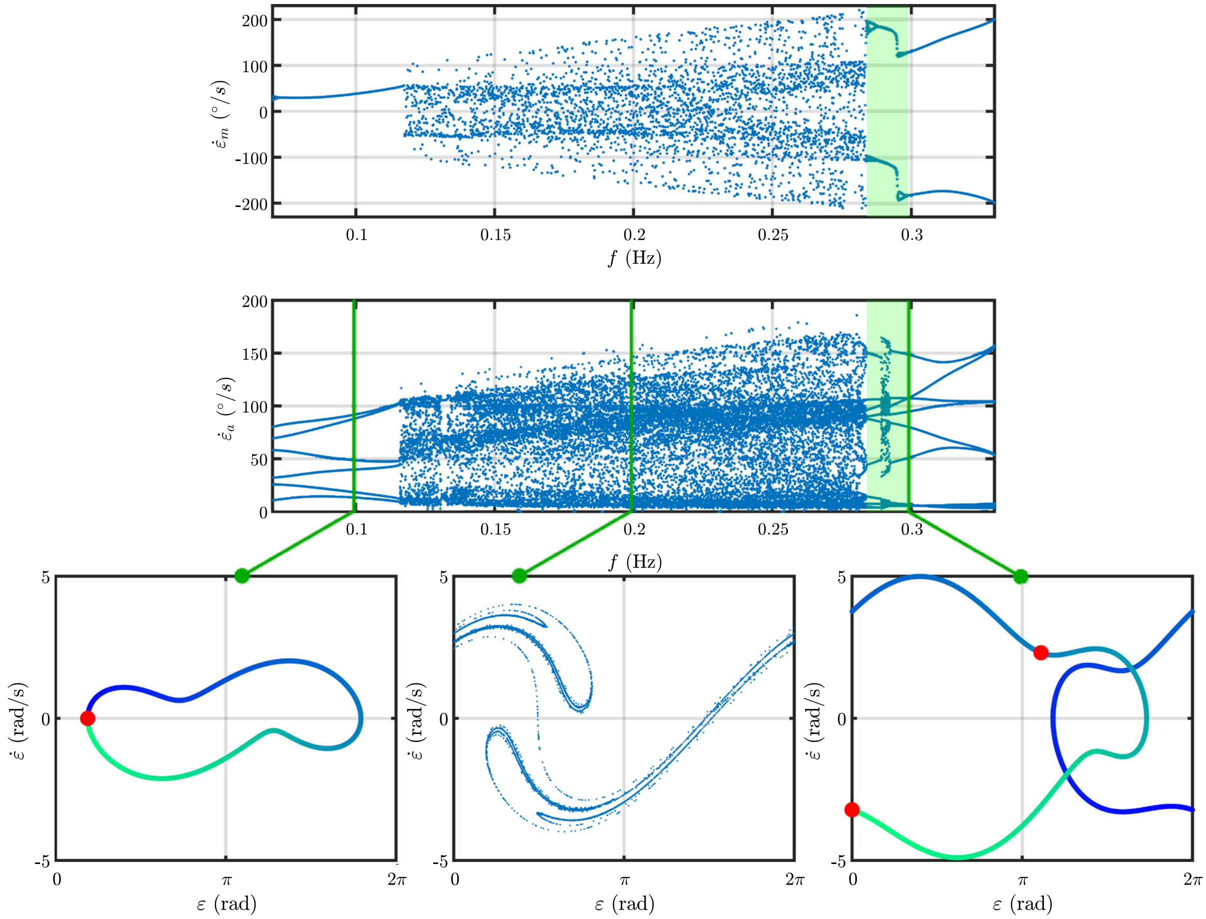

Fig. 8 Response to down-chirp pitch prescribed motion of amplitude equal to 8°: the top graph represents sampling at the peaks of the chirp signal; the bottom graph represents consecutive semi-distances between extremes (peaks of troughs); bottom phase portraits represent the response to harmonic prescribed motion at 0.1 Hz (left), 0.2 Hz (middle), and 0.3 Hz (right), with the color of the line proportional to time and the red markers are taken at the frequency of excitation when the response is periodic (left and right plots)

lowest and highest frequencies have 1 and 2 branches of $\dot{\varepsilon}_m$, respectively. Transitions from periodic to chaotic regimes seem abrupt; likewise, there are some jumps also along the periodic branches, i.e. just below 0.3 Hz.

Note that the single branch of $\dot{\varepsilon}_m$ corresponds to six branches of $\dot{\varepsilon}_a$: while the number of branches of $\dot{\varepsilon}_m$ determines the periodicity of the response, $\dot{\varepsilon}_a$ indicates the smoothness of the power production; since they can be both equivalently used to study the transition to chaos, hereafter the focus is shifted on $\dot{\varepsilon}_a$ only, which can also be used to identify regimes of oscillation or rotation, if combined with $\bar{\dot{\varepsilon}}$ (see later in the section).

Up- and down-chirps are compared in Fig. 9: small differences are found between the responses to up- and down-chirps, mostly within the shaded region up to 0.3 Hz. This substantial lack of significant hysteresis phenomena has been remarked also with other amplitudes of prescribed motion; therefore, all other results hereafter are obtained with up-chirp signals only.

Figure 8 also highlights the response to long harmonic prescribed motion at three representative frequencies in the phase plane: at 0.1 Hz (bottom-left), 0.2 Hz (bottom-center), and 0.3 Hz (bottom-right). In particular, since the response at 0.1 Hz and 0.3 Hz is periodic, phase plots are presented, with the color gradient proportional to time; moreover, these Poincaré maps include a red circular marker at each period of the exciting motion: consistently with the time

Fig. 9 Response to up- and down-chirp pitch prescribed motion of amplitude equal to 8°: the green shadowed area highlights when (small) differences are found between the two responses

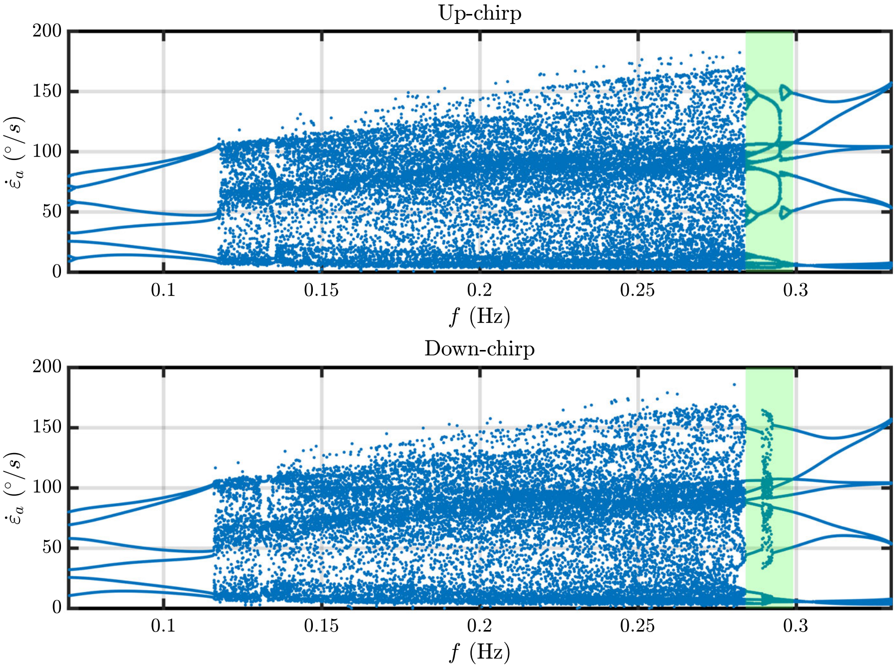

traces of Fig. 7, period doubling is found at 0.3 Hz, while the response at 0.1 Hz preserves the excitation period; multiple harmonics are also evident from the deformed shape of the phase plot. Focusing on the chaotic response at 0.2 Hz, the bottom-center phase plot presents a stroboscopic map across the entirety of the time trace; plotting one marker sampled at each excitation period, a classic strange attractor is found.

The effect of the amplitude of the external forcing is also considered, since it is to be expected that nonlinearities are strongly dependent on the magnitude of both the prescribed motion and the system's response. Fig. 10 groups together several response amplitudes ($\dot{\varepsilon}_a$) to up-chirp signals with constant amplitude, ranging from 4 to 16 degrees, with 1 degree increase; the color gradient is proportional to θ_a. Two main regions of apparently chaotic motion can be remarked, whose boundaries shift to higher frequencies as the forcing amplitude increases; similarly, the region of periodic motion in between the chaos regions appears to increase in size as the forcing amplitude increases, suggesting that the driving motion becomes able to override the chaotic motion of the system. Finally, the number of branches of the periodic region seem to change, according to the amplitude and frequency of the excitation motion; notably, for the smallest amplitudes of 4° and 5°, a single branch can be appreciated at the highest frequencies, with a bifurcation into 4 branches at lower frequencies.

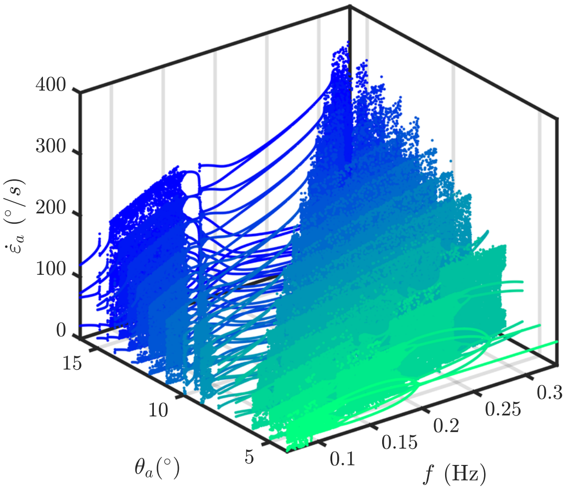

Fig. 10 Multiple free responses ($c_{PTO} = 0$) subject to up-chirp prescribed motions of constant amplitude, ranging from 4 to 16 degrees. The color gradient is proportional to θ_a

A clearer picture of the chaotic regions and the number of branches is produced in Fig. 11, which is built upon the time series of $\dot{\varepsilon}_a$ shown in Fig. 10. For every i-th point in the time series (p_i), the following point is sought that lies on the same branch, such that the relative difference between p_{i+N} and p_i is lower than

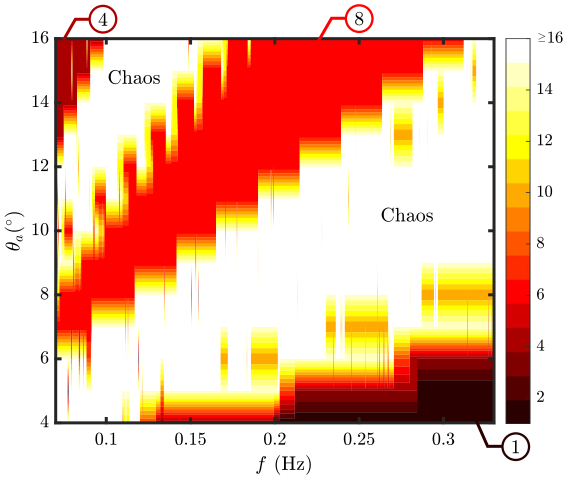

Fig. 11 Number of branches of the time series plotted in Fig. 10. The region is defined chaotic if the number of branches is more than 16

0.5%; once this condition is found, it is further verified with p_{i+2N} and p_{i+3N}, to confirm that the number of branches at the i-th frequency is indeed N. Note that this approach has been defined to be robust to abrupt changes of regimes as well as chaotic regions. Fig. 11 shows the results of this analysis, with seemingly chaotic regions identified when the number of branches is higher than 16. It should be noted that the presence of a large number of branches, corresponding to local maxima, does not necessarily imply that a motion is chaotic. Additionally, the threshold of 16 branches is arbitrary. Nevertheless, numerical results show that the chosen threshold of 16 is a good representation of the passage from a small number of branches to a very large number of branches; therefore, a larger threshold number would provide results with negligible quantitative differences. Additionally, although no rigorous analysis of the chaotic nature of the motion was performed, such as Lyapunov exponent analysis or fractal dimension of the attractors, the visual inspection of some of the attractors, like the one in Fig. 8 bottom-middle panel, clearly suggests that the motions are indeed chaotic. Furthermore, from an engineering perspective, a seemingly chaotic motion and a rigorously chaotic motion are practically equivalent, which suggests that the used methodology is appropriate.

Figure 11 highlights that there is a small region with a single branch, namely at low amplitude and high frequency; an even smaller region of 4 branches appears instead at the highest amplitude and smallest frequency. The largest region of periodic solutions has 8 branches; its width increases as the frequency increases, since its highest boundary is steeper than the lowest. Interestingly, both boundaries show a sawtooth profile; however, while the width of the steps is constant for the lower boundary, it is variable for the upper boundary, with the teeth of the periodic region becoming wider at the expenses of the upper chaotic region as the frequency increases. Finally, the lower and wider chaotic region shows localized areas with periodic solution at high number of branches.

The analysis of chaotic, and especially rotational and oscillatory regimes, are most relevant for the energy harvesting capability of the system. Sect. 4.3 and results therein are specifically addressing this topic.

4.3 Damped dynamics with energy extraction

Section 4.2 confirms the presence of interesting regions of the free response of the mechanism, namely where a sustained periodic motion has the potential to provide a predictable source of mechanical energy to be extracted. The current section has the objective to introduce the damping action of the PTO system, essential for power extraction, and verify how it affects the resulting dynamics. To do so in a compact and computationally efficient way, for each harmonic motion prescribed, a long-time simulation has been performed with c_{PTO} linearly and slowly varying with time along a constant slope. Results are shown in Fig. 12, considering a forcing amplitude of 8°.

The red line in the top graph of Fig. 12 shows the set of optimal c_{PTO} such that the mean power (P) is maximized. Since the variations of the instantaneous power follow the same periodicity of $\dot{\varepsilon}$, including the case of chaotic motions, the mean power to be maximized is defined as the moving average across a window large enough to appreciate the potentially complex dynamics of the system; this moving time window has been chosen to be 24 times the forcing period T, in order to be an integer multiple of superharmonics up to the 8th order. The resulting optimal c_{PTO} decreases with larger forcing periods. The top graph of Fig. 12 also differentiates the regions of pure rotation (where the velocity never changes sign) from the regions of oscillations (where the velocity systematically alternates sign, regardless of the periodicity).

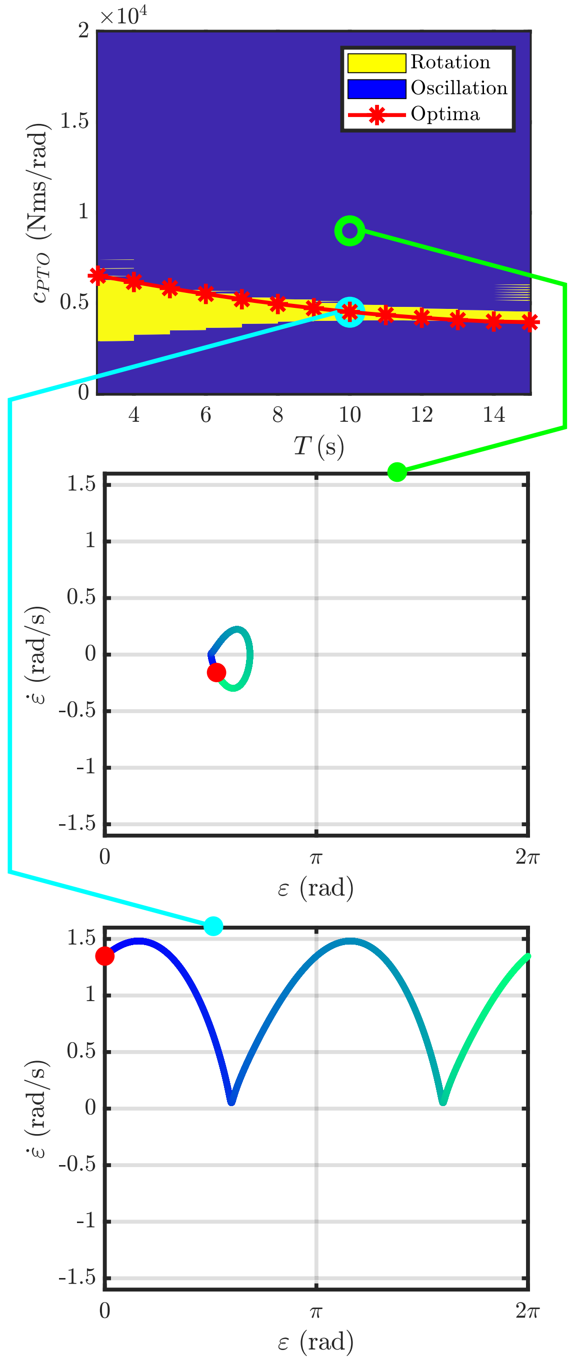

Fig. 12 Response to harmonic prescribed motion of period T and amplitude equal to 8°. The top graph shows the optimal c_{PTO} generating the highest power extraction, as well as regions of oscillation and pure rotations. Middle and bottom phase plots show examples of oscillation and rotation, respectively, with color gradient proportional to time and red marker sampled at the forcing period

It can be remarked that the optimal power extraction is always found in the region of pure rotation: since $\dot{\varepsilon}$ never changes sign, the instantaneous power is never zero, hence favoring a higher P; conversely, in a oscillation regime, the instantaneous power systematically is zero when $\dot{\varepsilon}$ changes sign. The favourability of the rotation regime is also found in systems like the parametric pendulum [49]. The center and bottom phase plots of Fig. 12 show representative examples of oscillation and rotation regimes, respectively, for close choices of c_{PTO}. Finally, it is worth noting that, in the top graph of Fig. 12, the rotation region gradually shrinks as the forcing period increases, making the choice of c_{PTO} more sensitive, thereby highlighting potential robustness issue of the control action.

While the focus of this analysis is on maximizing energy extraction, it is crucial to acknowledge the practical implications regarding mechanical wear and system longevity. Optimal power production in rotational regimes, where the PTO velocity maintains a consistent sign, suggests continuous operation of the power take-off and bearing components. This continuous motion, while maximizing power output, may induce consistent stresses on bearings and other mechanical components over extended periods. Conversely, in oscillatory regimes, where the velocity systematically changes sign, the instantaneous power becomes zero at velocity reversals. While leading to intermittent power extraction, such alternating motion can subject the system to repetitive loads and frequent reversals of direction. These dynamic reversals can accelerate wear on specific components and potentially lead to higher fatigue, particularly exacerbated by potential stick-slip friction due to improper lubrication. Therefore, a comprehensive design and optimization strategy for such wave energy converters must consider a trade-off between maximizing instantaneous or average power output and ensuring the long-term mechanical integrity and lifespan of the system. Future experimental work and full-scale prototype development will be essential to quantify these wear mechanisms and inform the selection of optimal PTO damping not only for maximum power but also for enhanced robustness and cost-effectiveness over the device's operational lifetime.

A closer look to the actual response to a prescribed harmonic motion with slowly-varying c_{PTO} is provided in Fig. 13, considering the example of forcing amplitude of 8° and period of 5 s. The top and center graph show the amplitude ($\dot{\varepsilon}_a$) and mean ($\overline{\dot{\varepsilon}}$) of $\dot{\varepsilon}$,

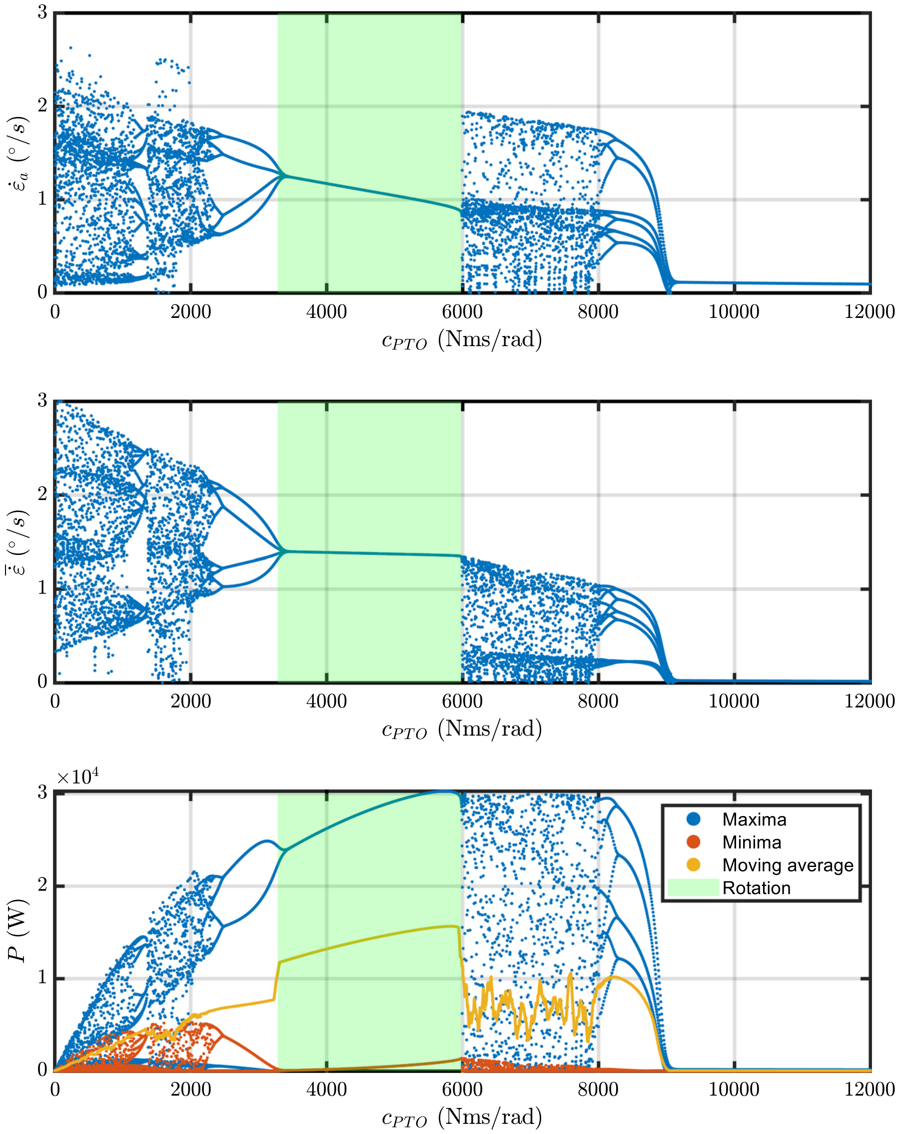

Fig. 13 Response to prescribed harmonic motion with θ_a of 8° and T of 5 s, with c_{PTO} linearly changing with time. The top and center graph show the amplitude and mean of $\dot{\varepsilon}$, respectively. The bottom graph shows the maxima, minima and moving average power. In all graphs, the area of rotation is shadowed, determined where the minima of the minima of the power are strictly greater than zero, or alternatively where $\dot{\varepsilon}_a \leq \bar{\dot{\varepsilon}}$

respectively. The unloaded response with no external damping ($c_{PTO} = 0$) is chaotic, and remains so until about 2,000 Nms/rad, apart from a narrow window of periodicity. Beyond 2,000 Nms/rad, a large periodic region is found, firstly with 4 branches, then with a single branch. Moreover, a regime of rotation can be identified at the single branch, since $\dot{\varepsilon}_a \leq \bar{\dot{\varepsilon}}$, which is the most convenient regime for power extraction. This result confirms that a chaotic region in the unloaded response (as analyzed in Sect. 4.2) can become periodic when the proper external action is applied; this could be a constant damping coefficient, as in this case, or a more elaborate external control action, purposely designed to maximise energy extraction. However, it is interesting to note that further increasing the damping action of the PTO leads the system back to chaos, specifically between 6,000 and 8,000 Nms/rad; this result serves as a warning and a reminder that just increasing the damping may not be an effective action to avoid a chaotic regime. Moreover, the jump from periodic to chaotic regimes, happening at 6,000 Nms/rad, is sudden and abrupt, highlighting potential robustness issues. Finally, beyond 8,000 Nms/rad the system becomes periodic once again, until the damping action is so large to completely limit the rotation.

The bottom graph of Fig. 13 shows the resulting power extracted by the PTO, highlighting the maxima, minima, and moving average. Clearly starting from zero, when c_{PTO} is also 0, the maximum power increases until about 8,000 Nms/rad, and then drops back to zero when the damping is too high. The minima of the power are always equal to zero, when there is an oscillation regime, since the velocity systematically becomes zero as it changes sign; conversely, it is greater than zero when there is a rotation regime, as highlighted in Fig. 13. The moving average is smooth in the region of periodic motion, either oscillation of rotation; however, it becomes erratic within the regions of chaos. Therefore, although the maxima in the chaos region may be similar to the neighboring periodic region (e.g., around 6,000 Nms/rad), the consequent moving average is much lower; this result is a clear remark that the chaotic region is not favorable for energy harvesting, despite localized peaks of high power conversion. Having a periodic solution with multiple branches (e.g., at 3,000 Nms/rad) seems to cause a smaller, although not negligible, jump in the mean power conversion, which is mainly caused by the shift from oscillation to rotation regime. Finally, it is interesting to notice that the optimal c_{PTO} overall is just below 6,000 Nms/rad, within the rotation region but close to the boundary with the chaotic region; the abrupt change of regime and mean power conversion raises a further concern on the sensitivity to the control parameter c_{PTO}. In this respect, we note that several previous studies already highlighted that chaotic motions generally are less effective than periodic ones for energy harvesting [60,61], mostly because of the lower average vibration amplitude. Other technical issues for energy harvesting from chaotic motions are mainly related to their broad-spectrum motion and irregular behavior.

Analysis similar to Figs. 12 and 13 are performed for all forcing amplitudes. The resulting maximum achievable mean power in response to harmonic prescribed motion, and the related optimal c_{PTO} parameter, are shown in Fig. 14. Both P and c_{PTO} increase for lower forcing periods and higher forcing amplitudes. The range of optimal values of c_{PTO} is relatively narrow, with apparently smooth changes across the domain; conversely, the mean power shows steeper changes, with a relatively small region having values close to the global maximum. This result suggests the need for a holistic optimization of the system's parameters to match the frequencies of interest; however, such an optimization lies beyond the scope of this paper, which is to study the nonlinear dynamics of the mechanism and to verify its underlying potential for energy harvesting.

5 Conclusions

This paper has analyzed the nonlinear dynamics of a mechanism for energy harvesting, composed of a flywheel with horizontal axis excited by prescribed motions in the pitching degree of freedom. The paper has presented and compared both a block-based and an analytical Lagrangian model with quasi-coordinates. The primary objective has been to describe both the free (undamped) and damped regions of motion in order to assess the potential for power conversion. The paper demonstrates the presence of both chaotic and periodic solutions, subject to different environmental conditions (prescribed motion amplitude and frequency) and tuning parameters (damping of the power take-off system). On the one hand, periodic solutions, and even more rotational solutions, are found to be the most promising for energy harvesting; on the other hand, the demonstrated sensitivity to design and control parameters lays the foundation for further work on holistic design [62] and optimal control [63]. A notable result highlighted in this paper is the sensitivity issue of the optimal parameters and the consequent abrupt changes of performance at the boundaries of periodic and chaotic regions, which may pose a peculiar challenge to both optimization design and control [64]. Furthermore, results presented in this paper must be further corroborated by including flywheel and bearings losses, mechanical coupling between the inertial mechanism and the hosting structure [65], as well as the analysis of more realistic panchromatic external excitation [66], which may, in principle, modify the onset of instability and chaos [58]. Finally, experimental validation at prototype level is required to validate the numerical results. In the small-scale prototyping phase, particular care should be taken on the relatively higher importance of friction, as well as smaller time-scales for actuation and control; furthermore, the dry-test research infrastructure should be able, in hardware-in-the-loop, to prescribe motion in multiple degrees of freedom, e.g. using a multi-axis hexapod or Stewart platform.

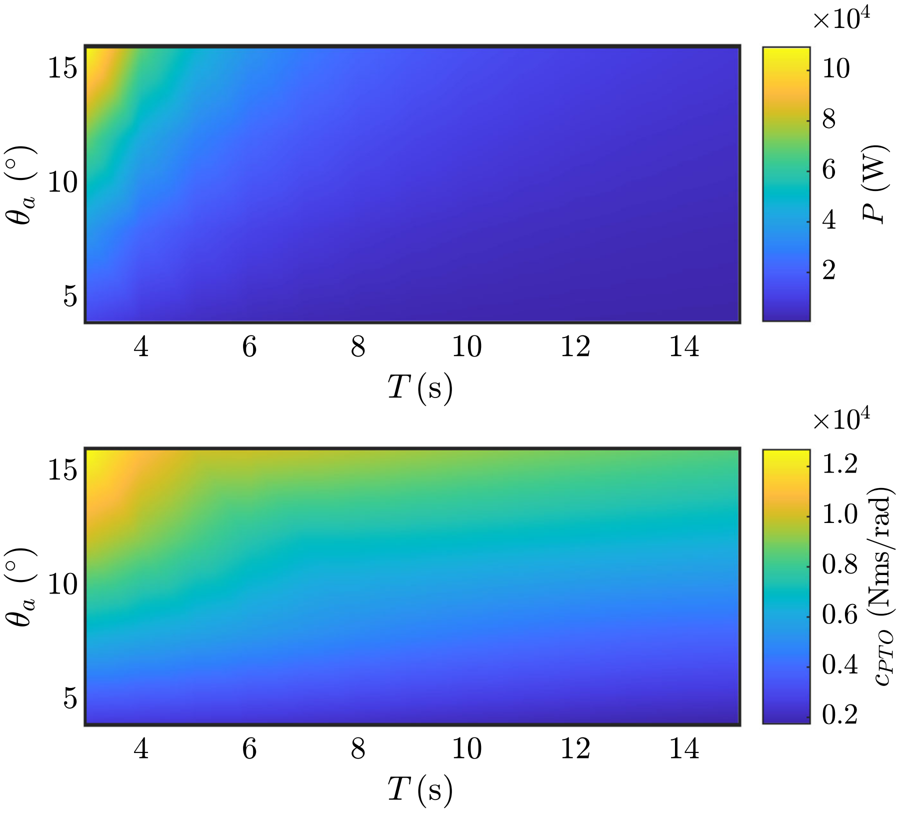

Fig. 14 Maximum mean power (top) and related optimal c_{PTO} (bottom) for every harmonic motion prescribed

Author contributions Conceptualization: G.G., F.C.; Methodology: G.G., G.H, F.C.; Software: G.G., F.C.; Validation: G.G., F.C.; Formal analysis: G.G., G.H, F.C.; Investigation: G.G.; Resources: G.G.; Data Curation: G.G.; Writing - Original Draft: G.G., F.C.; Writing - Review & Editing: G.G., F.C.; Visualization: G.G., G.H, F.C.; Supervision: G.H,F.C.; Project administration: G.G.; Funding acquisition: G.G.

Funding Project funded by the European Union – NextGenerationEU Award Number: Project code PE0000021, Concession Decree No. 1561 of 11.10.2022 adopted by Ministero dell'Universitá e della Ricerca (MUR), Italy, CUP, Italy E13C22001890001, Project title "Network 4 Energy Sustainable Transition – NEST".

References

1. Raimi, D., Campbell, E., Newell, R., Prest, B., Villanueva, S., Wingenroth, J.: Global energy outlook 2022: turning points and tension in the energy transition. Resources for the Future: Washington, DC, USA (2022)
2. Hansen, K., Mathiesen, B.V., Skov, I.R.: Full energy system transition towards 100% renewable energy in germany in 2050. Renew. Sustain. Energy Rev. **102**, 1–13 (2019)
3. Drew, B., Plummer, A.R., Sahinkaya, M.N.: A review of wave energy converter technology. Proc. Inst. Mech. Eng., Part A: J Power Energy **223**(8), 887–902 (2009). https://doi.org/10.1243/09576509jpe782
4. Falcão, AFd.O.: Wave energy utilization: A review of the technologies. Renew. Sustain. Energy Rev. **14**(3), 899–918 (2010). https://doi.org/10.1016/j.rser.2009.11.003
5. Gunn, K., Stock-Williams, C.: Quantifying the global wave power resource. Renewable Energy **44**, 296–304 (2012). https://doi.org/10.1016/j.renene.2012.01.101
6. Guo, B., Wang, T., Jin, S., Duan, S., Yang, K., Zhao, Y.: A Review of Point Absorber Wave Energy Converters. J. Mar. Sci. Eng. **10**(10), 1534 (2022). https://doi.org/10.3390/jmse10101534
7. Bouhrim, H., El Marjani, A., Nechad, R., Hajjout, I.: Ocean wave energy conversion: A review. J. Mar. Sci. Eng. **12**(11), 1922 (2024). https://doi.org/10.3390/jmse12111922
8. Ahmed, A., Yang, L., Huang, J., Shalaby, A., Datla, R., Zuo, L., Hajj, M.: Performance characterization and modeling of an oscillating surge wave energy converter. Nonlinear Dyn. **112**, 4007–4025 (2024). https://doi.org/10.1007/S11071-023-09248-2/TABLES/9
9. Rava, M., Dafnakis, P., Martini, V., Giorgi, G., Orlando, V., Mattiazzo, G., Bracco, G., Gulisano, A.: Low-cost heaving single-buoy wave-energy point absorber optimization for sardinia west coast. J. Mar. Sci. Eng. **10**(3), 397 (2022). https://doi.org/10.3390/jmse10030397
10. McNatt, J.C., Retzler, C.H.: The performance of the mocean m100 wave energy converter described through numerical

and physical modelling. Int. Mar. Energy J. **3**(1), 11–19 (2020)

11. Giglio, E., Petracca, E., Paduano, B., Moscoloni, C., Giorgi, G., Sirigu, S.A.: Estimating the Cost of Wave Energy Converters at an Early Design Stage: A Bottom-Up Approach. Sustainability **15**(8), 6756 (2023). https://doi.org/10.3390/su15086756
12. Wang, H., Sun, J., Xi, Z., Dai, S., Xing, F., Xu, M.: Recent progress on built-in wave energy converters: A review. J. Mar. Sci. Eng. **12**(7), 1176 (2024). https://doi.org/10.3390/jmse12071176
13. Wang, T.: Pendulum-based vibration energy harvesting: Mechanisms, transducer integration, and applications. Energy Convers. Manage. **276**, 116469 (2023). https://doi.org/10.1016/j.enconman.2022.116469
14. Giorgi, G.: Embedding parametric resonance in a 2:1 wave energy converter to get a broader bandwidth. Renewable Energy **222**, 119928 (2024). https://doi.org/10.1016/j.renene.2023.119928
15. Cordonnier, J., Gorintin, F., De Cagny, A., Clément, A.H., Babarit, A.: SEAREV: Case study of the development of a wave energy converter. Renewable Energy **80**, 40–52 (2015). https://doi.org/10.1016/j.renene.2015.01.061
16. Guo, B., Ringwood, J.V.: Non-Linear Modeling of a Vibro-Impact Wave Energy Converter. IEEE Trans. Sustain. Energy **12**(1), 492–500 (2021). https://doi.org/10.1109/TSTE.2020.3007926
17. Clemente, D., Rosa-Santos, P., Taveira-Pinto, F., Martins, P.: Influence of platform design and power take-off characteristics on the performance of the E-Motions wave energy converter. Energy Convers. Manage. **244**, 114481 (2021). https://doi.org/10.1016/j.enconman.2021.114481
18. Matos, C., Rosales-Asensio, E., Carta, J.A., Cabrera, P.: Flywheels in renewable energy systems: An analysis of their role in managing intermittency. J. Energy Storage **122**, 116674 (2025). https://doi.org/10.1016/j.est.2025.116674
19. Perez, T., Santos-Mujica, M., Ruiz-Minguela, J.P.: Performance analysis and control design of a gyro-based wave energy converter. 2009 European Control Conference, ECC 2009, 3743–3748 (2014) https://doi.org/10.23919/ECC.2009.7074982
20. Pei, Z., Jing, H., Tang, Z.: Modeling and Test Results of an Innovative Gyroscope Wave Energy Converter. Appl. Sci. **11**(10), 4359 (2021). https://doi.org/10.3390/app11104359
21. Modelling of the witt wave energy converter. Renewable Energy **115**, 159–174 (2018) https://doi.org/10.1016/J.RENENE.2017.08.004
22. Carapellese, F., Pasta, E., Sirigu, A.S., Faedo, N.: SWINGO: Conceptualization, modelling and control of a swinging omni-directional Wave Energy Converter. Mech. Syst. Signal Process. **197**, 110356 (2023)
23. Faraggiana, E., Chapman, J., Masters, I.: Influence of directional wave spreading on a wec device. Inter. Mar. Energy J. **5**, 227–242 (2022). https://doi.org/10.36688/IMEJ.5.227-242
24. Paduano, B., Faedo, N., Mattiazzo, G.: On the effect of wave direction on control and performance of a moored pitching wave energy conversion system. J. Mar. Sci. Eng. **11**, 2001 (2023). https://doi.org/10.3390/JMSE11102001
25. Carapellese, F., Clerck, V.D., Sirigu, S.A., Giorgi, G., Bonfanti, M., Faedo, N., Giorcelli, E.: Multi-objective optimization of an inertial wave energy converter for multi-directional wave scatter. Machines **12**, 736 (2024). https://doi.org/10.3390/MACHINES12100736
26. Bakhtiar, S., Khan, F.U., Fu, H., Hajjaj, A.Z., Theodossiades, S.: Fluid flow-based vibration energy harvesters: A critical review of state-of-the-art technologies. Appl. Sci. **14**(23), 11452 (2024). https://doi.org/10.3390/app142311452
27. Aderinto, T., Li, H.: Ocean wave energy converters: Status and challenges. Energies **11**(5), 1250 (2018)
28. Bonfanti, M., Sirigu, S.A., Giorgi, G., Dafnakis, P., Bracco, G., Mattiazzo, G.: A passive control strategy applied to the iswec device: Numerical modelling and experimental tests. Int. J. Mech. Control (2020)
29. Ghouli, Z., Litak, G.: Effect of high-frequency excitation on a bistable energy harvesting system. J. Vib. Eng. Technol. **11**, 99–106 (2023). https://doi.org/10.1007/S42417-022-00562-4
30. Blanco, M., Torres, J., Santos-Herrán, M., García-Tabarés, L., Navarro, G., Nájera, J., Ramírez, D., Lafoz, M.: Correction to: Recent Advances in Direct-Drive Power Take-Off (DDPTO) Systems for Wave Energy Converters Based on Switched Reluctance Machines (SRM), pp. 1–1 (2022). https://doi.org/10.1007/978-3-030-78716-5_19
31. Sirigu, A.S., Gallizio, F., Giorgi, G., Bonfanti, M., Bracco, G., Mattiazzo, G.: Numerical and Experimental Identification of the Aerodynamic Power Losses of the ISWEC. J. Mar. Sci. Eng. **8**(1), 49 (2020). https://doi.org/10.3390/jmse8010049
32. Miles, M.D., Funke, E.R.: A Comparison of Methods for Synthesis of Directional Seas. J. Offshore Mech. Arct. Eng. **111**(1), 43–48 (1989). https://doi.org/10.1115/1.3257137
33. Pasta, E., Carapellese, F., Paduano, B., Glorioso, M., Papini, G., Faedo, N., Mattiazzo, G., Lomonaco, P.: Preliminary Results of the Experimental Assessment of the SWINGO Wave Energy System, pp. 183–191 (2025). https://doi.org/10.1201/9781003558859-21
34. Bonfanti, M., Giorgi, G.: Improving Computational Efficiency in WEC Design: Spectral-Domain Modelling in Techno-Economic Optimization. J. Mar. Sci. Eng. **10**(10), 1468 (2022). https://doi.org/10.3390/jmse10101468
35. Carapellese, F., Pasta, E., Faedo, N., Giorgi, G.: Dynamic analysis and performance assessment of the Inertial Sea Wave Energy Converter (ISWEC) device via harmonic balance. In: 14th IFAC Conference on Control Applications in Marine Systems, Robotics and Vehicles, Lyngby, Denmark (2022)
36. Faedo, N., Peña-Sanchez, Y., Ringwood, J.V.: Finite-order hydrodynamic model determination for wave energy applications using moment-matching. Ocean Eng. **163**, 251–263 (2018). https://doi.org/10.1016/j.oceaneng.2018.05.037
37. Carapellese, F., Pasta, E., Paduano, B., Faedo, N., Mattiazzo, G.: Intuitive LTI energy-maximising control for multi-degree of freedom wave energy converters: The PeWEC case. Ocean Eng. **256**, 111444 (2022). https://doi.org/10.1016/j.oceaneng.2022.111444
38. Faedo, N., Bussi, U., Peña-Sanchez, Y., Windt, C., Ringwood, J.V.: A simple and effective excitation force estimator for wave energy systems. IEEE PES Trans. Sustain. Energy **13**(1), 241–250 (2021)

39. Faedo, N., Peña-Sanchez, Y., Carapellese, F., Mattiazzo, G., Ringwood, J.V.: LMI-based passivisation of LTI systems with application to marine structures (2021). https://doi.org/10.1109/TSTE.2021.3108576
40. Dotti, F.E., Virla, J.N.: Nonlinear Dynamics of the Parametric Pendulum With a View on Wave Energy Harvesting Applications. J. Comput. Nonlinear Dyn. **16**(6), 061007 (2021). https://doi.org/10.1115/1.4050699
41. Carapellese, F., Paduano, B., Pasta, E., Papini, G., Faedo, N., Mattiazzo, G.: Nonlinear dynamic analysis and control synthesis for the Swinging Omnidirectional (SWINGO) Wave Energy Converter. IFAC-PapersOnLine **56**(2), 11723–11728 (2023). https://doi.org/10.1016/j.ifacol.2023.10.540
42. Carapellese, F., Faedo, N.: Mechanical interactions modeling of inertial wave energy converters. Int. J. Mech. Sci. **284**, 109731 (2024). https://doi.org/10.1016/j.ijmecsci.2024.109731
43. Genta, G.: Vibration Dynamics and Control. Mechanical Engineering Series. Springer, Boston, MA (2009). https://doi.org/10.1007/978-0-387-79580-5
44. Meirovitch, L.: Hybrid state equations of motion for flexible bodies in terms of quasi-coordinates. J. Guid. Control. Dyn. **14**(5), 1008–1013 (1991). https://doi.org/10.2514/3.20743
45. Siciliano, B., Sciavicco, L., Villani, L., Oriolo, G.: Robotics: Modeling, Planning, and Control. Advanced Textbooks in Control and Signal Processing. Springer, London (2009). https://doi.org/10.1007/978-1-84628-642-1
46. Meirovitch, L.: Methods of Analytical Dynamics. McGraw-Hill, Mineola, New York (1970)
47. Faedo, N., Scarciotti, G., Astolfi, A., Ringwood, J.V.: Nonlinear Energy-Maximizing Optimal Control of Wave Energy Systems: A Moment-Based Approach. IEEE Trans. Control Syst. Technol. **29**(6), 2533–2547 (2021). https://doi.org/10.1109/TCST.2020.3047229
48. Merigaud, A., Ringwood, J.V.: Free-Surface Time-Series Generation for Wave Energy Applications. IEEE J. Oceanic Eng. **43**, 19–35 (2018). https://doi.org/10.1109/JOE.2017.2691199
49. Xu, X., Wiercigroch, M., Cartmell, M.P.: Rotating orbits of a parametrically-excited pendulum. Chaos, Solitons Fractals **23**(5), 1537–1548 (2005). https://doi.org/10.1016/j.chaos.2004.06.053
50. The MathWorks Inc: Simscape™ Getting Started Guide (2023)
51. Jordan, D.W., Smith, P.: Nonlinear Ordinary Differential Equations: An Introduction for Scientists and Engineers. Oxford University Press, Oxford (2007)
52. Cervelli, G., Parrinello, L., Moscoloni, C., Giorgi, G.: Comparison of the era5 wave forecasting dataset against buoy record. Instrum. Mes. Metrol. **21**(3), 87–95 (2022). https://doi.org/10.18280/i2m.210301
53. Xia, X.-G.: System identification using chirp signals and time-variant filters in the joint time-frequency domain. IEEE Trans. Signal Process. **45**(8), 2072–2084 (1997)
54. Pierson, W.J., Moskowitz, L.: A proposed spectral form for fully developed wind seas based on the similarity theory of S. A. Kitaigorodskii. J. Geophys. Res. **69**(24), 5181–5190 (1964). https://doi.org/10.1029/JZ069i024p05181
55. Hasselmann, K.: Measurements of wind wave growth and swell decay during the Joint North Sea Wave Project (JONSWAP)', (1973)
56. Paduano, B., Carapellese, F., Pasta, E., Sirigu, S.A., Faedo, N., Mattiazzo, G.: Data-based control synthesis and performance assessment for moored wave energy conversion systems: The pewec case. IEEE Trans. Sustain. Energy **15**, 355–367 (2024). https://doi.org/10.1109/TSTE.2023.3285016
57. Vervaet, T., Quartier, N., Carpintero Moreno, E., Verao Fernandez, G., Ferri, F., Stratigaki, V., Troch, P.: System identification and centralised causal impedance matching control of a row of two heaving point absorber wave energy converters. Ocean Eng. **309**, 118399 (2024). https://doi.org/10.1016/j.oceaneng.2024.118399
58. Giorgi, G.: The onset of instability in a parametric resonance energy harvester under panchromatic excitations. Int. J. Mech. Sci. **281**, 109544 (2024). https://doi.org/10.1016/j.ijmecsci.2024.109544
59. Habib, G., Giorgi, G., Davidson, J.: Coexisting attractors in floating body dynamics undergoing parametric resonance. Acta Mech. **233**(6), 2351–2367 (2022). https://doi.org/10.1007/s00707-022-03225-3
60. Litak, G., Friswell, M.I., Adhikari, S.: Regular and chaotic vibration in a piezoelectric energy harvester. Meccanica **51**(5), 1017–1025 (2015). https://doi.org/10.1007/s11012-015-0287-9
61. Margielewicz, J., Gąska, D., Litak, G., Wolszczak, P., Zhou, S.: Energy harvesting in a system with a two-stage flexible cantilever beam. Sensors **22**(19), 7399 (2022). https://doi.org/10.3390/s22197399
62. Ringwood, J.V.: Control co-design for wave energy systems. Appl. Ocean Res. **158**, 104514 (2025). https://doi.org/10.1016/j.apor.2025.104514
63. Giorgi, G., Faedo, N.: Performance enhancement of a vibration energy harvester via harmonic time-varying damping: A pseudospectral-based approach. Mech. Syst. Signal Process. **165**, 108331 (2022). https://doi.org/10.1016/j.ymssp.2021.108331
64. Fusco, F., Ringwood, J.V.: Hierarchical robust control of oscillating wave energy converters with uncertain dynamics. IEEE Trans. Sustain. Energy **5**, 958–966 (2014)
65. Costa, L.G., Savi, M.A., Costa, L.G., Savi, M.A.: Pendulum-based hybrid system for multidirectional energy harvesting. Nonlinear Dyn. **112**, 18665–18684 (2024). https://doi.org/10.1007/s11071-024-10040-z
66. Song, K., Bonnin, M., Traversa, F.L., Bonani, F.: Broadband vibration energy harvesting using nonlinear multi degree-of-freedom mechanical filters. Nonlinear Dyn. **113**, 14301–14317 (2025). https://doi.org/10.1007/S11071-025-10950-6/FIGURES/B